Electronic Supplementary Information

Two-Dimensional MoS_2/Fe-Phthalocyanine Hybrid Nanostructures as Excellent Electrocatalysts for Hydrogen Evolution and Oxygen Reduction Reactions

Ik Seon Kwon,[a,†] *In Hye Kwak,*[a,†] *Ju Yeon Kim,*[b,†] *Hafiz Ghulam Abbas*,[b] *Tekalign Terfa Debela,*[c] *Jaemin Seo,*[a] *Min Kyung Cho,*[d] *Jae-Pyoung Ahn,*[d] *Jeunghee Park,**[,a] *and Hong Seok Kang**[,e]

[a] Department of Chemistry, Korea University, Sejong 339-700, Republic of Korea; E-mail: parkjh@korea.ac.kr

[b] Department of Nanoscience and Nanotechnology, Jeonbuk National University, Chonju, Chonbuk 54896, Republic of Korea

[c] Institute for Application of Advanced Materials, Jeonju University, Chonju, Chonbuk 55069, Republic of Korea

[d] Advanced Analysis Center, Korea Institute of Science and Technology Seoul 136-791, Republic of Korea.

[e] Department of Nano and Advanced Materials, College of Engineering, Jeonju University, Chonju, Chonbuk 55069, Republic of Korea; E-mail: hsk@jj.ac.kr

[†] I.S.K., I.H.K., and J.Y.K. equally contribute.

Contents

IV. References

I. Experimental

Synthesis.

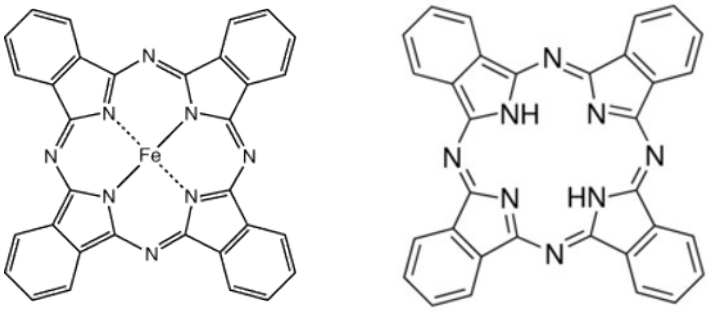

Scheme S1. Structures of Fe(II)-phthalocyanine (left) and 29H,31H-phthalocyanine (right), which are referred to as FePc and H_2Pc, respectively.

The structure of Fe(II)-phthalocyanine and 29H,31H-phthalocyanine is shown in **Scheme S1**.

Characterization. The products were characterized by scanning electron microscopy (SEM, Hitachi S-4700), and field-emission transmission electron microscopy (FE TEM, FEI TECNAI G2 200 kV, Jeol JEM 2100F, HVEM). Energy-dispersive X-ray fluorescence spectroscopy (EDX) with elemental maps was measured using a TEM (FEI Talos F200X) operated at 200 keV that equipped with high-brightness Schottky field emission electron source (X-FEG) and Super-X EDS detector system (Bruker Super-X). This EDX has powerful sensitivity and resolution in the low photon energy region. Fast Fourier-transform (FFT) images were generated by the inversion of the TEM images using Digital Micrograph GMS1.4 software (Gatan Inc.).

Cs-corrected STEM analysis was also carried out using a Titan 80-300^{TM} (FEI, The Netherlands) microscope operated at 300 kV. The STEM convergence semi-angle (α) used was ~18 mrad. The STEM minimum and maximum acceptance semi-angles (β) were ~20 and 122

mrad, respectively.

High-resolution X-ray diffraction (XRD) patterns were obtained using the 9B and 3D beamlines of the Pohang Light Source (PLS) with monochromatic radiation (λ = 1.54595 Å). XRD pattern measurements were also carried out in a Rigaku D/MAX-2500 V/PC using Cu K_α radiation (λ = 1.54056 Å). X-ray photoelectron spectroscopy (XPS) measurements were performed using the 8A1 beam line of the PLS, as well as a laboratory-based spectrometer (Thermo Scientific Theta Probe) using a photon energy of 1486.6 eV (Al Kα). X-ray absorption near edge spectra (XANES) and extended X-ray absorption fine structure (EXAFS) spectra at the Mo K-edge were collected in transmission mode using the 10C beam line of the PLS with a ring current of 350 mA at 3.0 GeV. Energy calibration was carried out by simultaneously measuring the reference spectrum of Mo metal foil. Least-squares fits of EXAFS data were performed using the Athena and Artemis software packages, version 0.9.25.

Solid-state ^{13}C (100.64 MHz) NMR spectra were acquired on a Bruker AVANCE II$^+$ 400 MHz NMR system (at the KBSI Seoul Western Center) equipped with a Bruker 3.2 mm bore HXY probe operating in HX mode. The magic angle spinning ^{13}C NMR experiments (one pulse method) were performed using a pulse length of 2 μs for a $\pi/2$ pulse length of 5 μs, and a pulse repetition delay time of 3 s. The spectra were referenced to an external adamantane standard in which the peak at higher chemical shift was set at 38.43 ppm. The spectra were processed using the Bruker Topspin software (version 3.2) using conventional techniques, and a 50 Hz line broadening window function was applied in all cases. Raman spectra were measured with a micro-Raman spectrometer (Horiba ARAMIS IR2), using a diode laser with an excitation wavelength of 532 nm.

N_2 adsorption-desorption isotherms were measured at 77 K on a Micromeritics Tristar 3000 analyzer. Before the measurements, the sample was degassed at 100 ºC for 24 h. The specific surface area was calculated via the Brunauer-Emmett-Teller (BET) model at relative pressures of $P/P_0 = 0.45$. The total pore volume was estimated from the uptake of adsorbate at a relative pressure of $P/P_0 = 0.99$. Pore size distributions were derived from the adsorption branches of the isotherms using the Barrett-Joyner-Halenda (BJH) model.

Electrochemical Measurements. Experiments were carried in a three-electrode cell connected to an electrochemical analyzer (CompactStat, Ivium Technologies). An Ag/AgCl electrode (saturated with 4M KCl, Pine Co.) or saturated calomel electrode (SCE, KCl saturated, Basi Model RE-2BP) was used as reference electrode. A graphite rod (6 mm dia. × 102 mm long, 99.9995%, Pine Instrument) was used as counter electrode. The applied potentials (E) reported in our work were referenced to the reversible hydrogen electrode (RHE) through standard calibration. In 0.1 M KOH electrolyte (pH 13), E (vs. RHE) = E (vs. SCE) + $E_{Ag/AgCl}$ (= 0.197 V) + 0.0592 pH = E (vs. Ag/AgCl) + 0.9606 V. In 0.5 M H_2SO_4 electrolyte (pH 0), E (vs. RHE) = E (vs. SCE) + E_{SCE} (= 0.241 V) + 0.0592 pH = E (vs. SCE) + 0.241 V.

For HER electrocatalysis, 4 mg sample was mixed with 1 mg carbon black (Vulcan XC-72) dispersed in Nafion (20 μL) and isopropyl alcohol (0.98 mL). The catalyst materials (0.390 mg cm^{-2}) were deposited on a glassy carbon (GC) rotating disk electrode (RDE, area = 0.1641 cm^2, Pine Instrument). The Pt/C (20 wt.% Pt in Vulcan carbon black, Aldrich-Sigma) tested as reference sample using the same procedure.

Linear sweeping voltammetry (LSV) of HER electrocatalysis in 0.5 M H_2SO_4 was measured from 0 to -0.8 V (vs. RHE) with a scan rate of 2 mV s^{-1}. A rotation speed of 1600 rpm was used. A saturated calomel electrode was used as reference electrode, and a graphite rod was

used as counter electrode. The electrolyte was purged with H_2 (ultrahigh grade purity) during the measurement. The applied potentials (E) reported in our work were referenced to the reversible hydrogen electrode (RHE) through standard calibration. For example, in 0.5 M H_2SO_4 electrolyte (pH 0), E (vs. RHE) = E (vs. SCE) + E_{SCE} (= 0.241 V) + 0.0592 pH = E (vs. SCE) + 0.241 V. The overpotential (η) was defined as E (vs. RHE).

Electrochemical impedance spectroscopy (EIS) measurements were carried out for the electrode in an electrolyte by applying an AC voltage of 10 mV in the frequency range of 100 kHz to 0.1 Hz at a bias voltage of -0.15 V (vs. RHE). To measure double-layer capacitance via cyclic voltammetry (CV), a potential range in which no apparent Faradaic processes occur was determined from static CV. This range is 0.1–0.2 V. All measured current in this non-Faradaic potential region is assumed to be due to double-layer capacitance. The charging current, i_c, is then measured from CVs at multiple scan rates. The working electrode was held at each potential vertex for 10 s before beginning the next sweep. The double-layer capacitance current density (J) is equal to the product of the scan rate (ν) and the electrochemical double-layer capacitance (C_{dl}), as given by equation $J = \nu C_{dl}$, Thus, a plot of J as a function of ν yields a straight line with a slope equal to C_{dl}. The scan rates were 20–100 mV s^{-1}.

For ORR electrocatalysis, 1 mg MoS_2 sample or FePc powder was mixed with 1 mg carbon black (Vulcan XC-72) dispersed in Nafion (20 μL) and isopropyl alcohol (0.98 mL). The catalyst materials (0.1 mg cm^{-2}) were deposited on a glassy carbon (GC) rotating disk electrode (RDE, area = 0.1641 cm^2, Pine Instrument). The Pt/C (20 wt.% Pt in Vulcan carbon black, Aldrich-Sigma) tested as reference sample using the same procedure.

The O_2 (ultrahigh grade purity) gas was bubbled with a flow rate of 20 sccm (mL min^{-1})

during the measurement. RDE measurements were performed at rotation speeds varying from 400 to 2500 rpm with a scan rate of 5 mV s^{-1} from 1.2 to 0 V (vs. RHE). The number of electrons involved in the ORR was calculated using the Koutecky–Levich (K–L) equation: $J^{-1} = J_L^{-1} + J_K^{-1} = (B\omega^{1/2})^{-1} + J_K^{-1}$, $B = 0.62nFC_0(D_0)^{2/3} n^{-1/6}$, and $J_K = nFkC_0$, where J is the measured current density, J_K and J_L are the kinetic- and diffusion-limiting current densities, ω is the angular velocity of the disk ($=2\pi N = 2\pi f/60$, where N is the linear rotation speed, and f is the RDE rotation rate in rpm), n is the overall number of electrons transferred in oxygen reduction, F is the Faraday constant (= 96485 C mol^{-1}), C_0 is the bulk concentration of O_2 ($=1.2 \times 10^{-6}$ mol cm^{-3}), n is the kinematic viscosity of the electrolyte ($=1.01\times10^{-2}$ cm^2 s^{-1}), and D_0 is the diffusion coefficient of O_2 at room temperature ($=1.97\times10^{-5}$ cm^2 s^{-1}). The number of electrons transferred (n) and J_K can be obtained from the slope and intercept of the K–L plots (J^{-1} *vs*. $\omega^{-1/2}$), respectively.

TOF H_2 Calculation. The active site density and per-site turnover frequency (TOF) have been estimated as follows. It should be emphasized that since the nature of the active sites of the catalyst is not clearly understood yet and the real surface area for the nanostructured heterogeneous catalyst is hard to accurately determine, the following result is really just an estimation.

To estimate the active surface site density, we used the C_{dl} value, and further calculate the electrochemically active surface area. The roughness factor (basically the surface area ratio between the catalyst vs. the metal electrodes (0.035 mF cm^{-2}),[S1] is 1006 (= 35.2 mF cm^{-2}/0.035 mF cm^{-2}) and 2400 (= 84.0 mF cm^{-2}/0.035 mF cm^{-2}) for H_2Pc-MoS_2 and FePc-MoS_2, respectively.

The number of catalytic sites on the surface of flat catalyst can be calculated based on the crystal structure of distorted octahedral-phase 1T' MoS_2. Using the lattice parameters of 1T' phase MoS_2 (we calculated as a = 3.27 Å, b = 3.17 Å, γ = 119°) and assuming one active site per MoS_2 (which translates into on reactive sites per unit cell), the density of surface active sites is: $1/(0.5 \times 3.17 \times 3.27 \times \sin 119°) \times 10^{16}$ cm^{-2} = 2.2×10^{15} atom cm^{-2}.[S2] Our DFT calculation shows that the basal S sites above the center site (H or Fe) of Pc (5%) are most active sites, so the number of surface active sites is calculated as $0.05 \times 2.2 \times 10^{15}$ atom cm^{-2} = 1.1×10^{14} atom cm^{-2}. The density of surface active sites (m) of H_2Pc-MoS_2 and H_2Pc-MoS_2 on geometric area: 1.1×10^{14} atom cm^{-2} × roughness factor = 1.11×10^{17} and 2.64×10^{17} atom cm^{-2}, respectively.

The total number of hydrogen (H_2) gas turns overs was calculated from the current density (J in mA cm^{-2}) according to n_{H2} = J (mA cm^{-2})/1000 mA × 1 C s^{-1} × 1 mol e$^-$/96486 C × (1 mol H_2/2 mol e^{-1}) × (6.022×10^{23} H_2 molecules/1 mol H_2) = 3.12×10^{15} H_2 s^{-1} cm^{-2} per mA cm^{-2}.

At η = 0.18 V, J = 29.2 and 177.5 mA cm^{-2} for H_2Pc-MoS_2 and FePc-MoS_2, respectively, provides the TOF as 0.82 and 2.1 H_2 s^{-1}.

We summarized the TOF values at 0.18 V as follows.

Samples	J (mA cm^{-2}) at 0.18 V	n_{H2}	Roughness factor	m	TOF
H_2Pc-MoS_2	29.2	9.1×10^{16}	1006	1.11×10^{17}	0.82
FePc-MoS_2	177.5	5.5×10^{17}	2400	2.64×10^{17}	2.1

Computation.

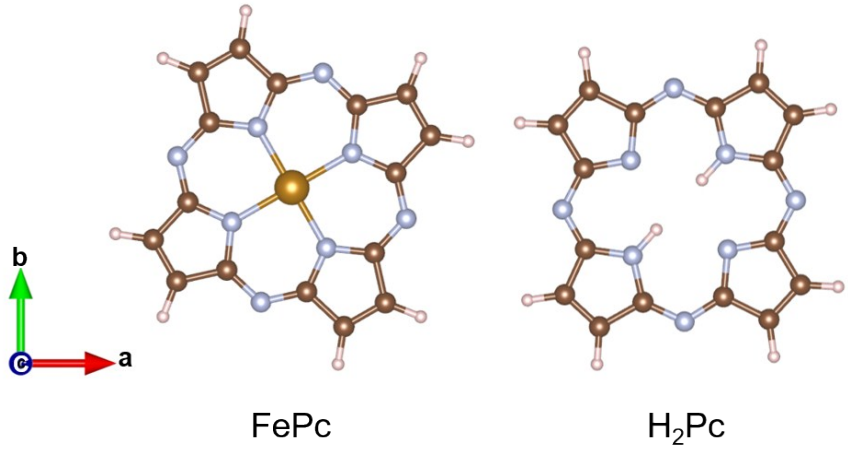

Scheme S2. Structures (ball and stick model) of FePc and H_2Pc used for calculation, where four phenyl rings of phthalocyanine molecules were substituted with H atoms.

II. Supporting Tables

Table S1. Fitting parameters of EXAFS data for the MoS_2 samples and FePc (see **Figure S5** and **Figures 2d and 2f**). The FT curves of EXAFS were fitted to two scattering shells. A least-squares curve parameter method was performed using the ARTEMIS module of IFEFFIT and USTCXAFS software packages.

	Sample	Scattering Path	R (Å)[a]	CN[b]	ΔE (eV)[c]	σ^2 (Å^2)[d]
Mo K-edge	2H-MoS_2	Mo-S	2.40	6.00	1.3	0.0028
		Mo-Mo	3.16	6.00	0.8	0.0036
	MoS_2	Mo-S	2.40	4.5 ± 0.4	-1.1	0.0077
		Mo-Mo	2.76	1.8 ± 0.7	1.5	0.0106
	H_2Pc-MoS_2	Mo-S	2.41	5.8 ± 0.9	-1.4	0.0080
		Mo-Mo	2.76	1.1 ± 0.7	-2.0	0.0072
	FePc-MoS_2	Mo-S	2.40	5.0 ± 0.6	-3.4	0.0078
		Mo-Mo	2.78	1.0 ± 0.5	4.9	0.0045
Fe K-edge	FePc	Fe-N/Fe-O	1.95	4.00	3.5	0.0133
	FePc-MoS_2	Fe-N/Fe-O	2.04	5.1 ± 0.4	1.7	0.0108

[a] Distance between scattering atoms. The FT curve of the 2H phase MoS_2 are characterized by two main peaks at 2.40 and 3.16 Å, corresponding to the nearest Mo–S and Mo–Mo bonds, respectively. In contrast, in the FT curves of H_2Pc-MoS_2 and FePc-MoS_2, the second peak

(related to the nearest Mo–Mo bond) shows a noticeable shift from 3.16 to 2.76-2.78 Å.

[b] Coordination number of Mo atoms. The intensity of this peak is nearly reduced by 1/3, corresponding to the coordination number of Mo-Mo decreased significantly. All these results indicate that the intercalated MoS_2 adopts a distorted octahedral coordination.

[c] Edge energy shift, representing between the energy grids of experimental and theoretical data.

[d] Debye-Waller factor, which measures the static and thermal disorder, is larger for 1T′ phase MoS_2 samples than 2H-MoS_2. It suggests that the intercalation produces a broad range of Mo-S and Mo-Mo distances.

Table S2. Impedance parameters for the equivalent circuit that was shown in **Figure S8**, and the double-layer capacitance (C_{dl}) as shown in **Figure S9**.

`	EIS		C_{dl} (mF cm^{-2})
Samples	R_s (Ω)	R_{ct} (Ω)	
FePc-MoS_2	4.0	8.5	84.0
H_2P-MoS_2	4.7	22.2	35.2
MoS_2	5.0	30.0	14.3

Table S3. BET specific surface area and BJH pore volume/average pore diameter of FePc-MoS_2 and MoS_2 samples derived from the N_2 adsorption-desorption isotherms.

Sample	S_{BET}(m^2 g^{-1})[a]	V_{BJH} (cm^3 g^{-1})[b]	D_{BJH} (nm)[c]
FePc-MoS_2	69.42	0.29	3.6
MoS_2	58.68	0.26	3.6

[a] BET specific surface area; [b] BJH pore volume; [c] BJH average pore diameter.

Table S4. Comparison of HER performance (in pH 0) of MoS_2 in the literatures.

Reference	Materials	Phase	$E_{J=10}$ (mV) at 10 mA cm^{-2}	Tafel slope (mV dec^{-1})	TOF (H_2 s^{-1})
S2	Mesoporous MoS_2	1T	154	43	0.5 at 0.153 V
S3	DMPD intercalated MoS_2	1T'	160	38	N/A
S4	Defect-rich MoS_2	2H	~190	50	0.725 at 0.3 V
S5	Conducting MoS_2 Nanosheets	1T	200	40	N/A
S6	Ammoniated MoS_2	2H	320	45	N/A
S7	Single layer MoS_2	2H	N/A	45	0.019-0.046 at 0 V
S8	Metallic-phase MoS_2 nanosheets	1T	175	41	N/A
S9	MoS_2 monolayer	1T'	300	61	3.8±1.6 at 0.077 V
S10	Multiphasic MoS_2	1T/2H	234	46	~ 0.15 at 0.2 V
S11	Functionalized MoS_2 nanosheets	1T	348	75	N/A
S12	MoSSe nanodots	1T	140	40	N/A
S13	S depleted MoS_2	2H	150 (at 6.5 mA cm^{-2})	38	8.74 at 0.2 V
S14	S vacancy rich surface MoS_2	2H	N/A	102	~9 at 0.2 V
S15	Zn doped MoS_2	2H	N/A	51	~ 5 at 0.2 V
S16	Pd doped MoS_2	1T	89	62	16.54 at 0.2 V
Present work	FePc-MoS_2	1T'	123	32	2.1 at 0.18 V

Table S5. Comparison of ORR performance (in pH 13) of MoS_2 and Fe-N_4 structures in the literatures.

Reference	Materials	Phase	$E_{1/2}$ (V vs. RHE)	Tafel slope (mV dec^{-1})	Loading (mg cm^{-2})
S17	MoS_2/N-doped carbon	2H	0.81	N/A	N/A
S18	MoS_2/ N-doped CNT	2H	0.82	N/A	0.3
S19	FePc- pyridyl groups-CNT	-	0.915	27	0.318
S20	FePc-MWCNT	-	0.864	36	0.3
S21	Pc-FePc complex on the Mn-modified graphitized carbon black	-	0.90	42	0.1
S22	FePc/$Ti_3C_2T_x$	-	0.89	N/A	0.25
S23	Au/Pyridinium/FePc	-	0.923	30	N/A
S24	CNT/PC (CNTs coated with thin layer of porphyrinic carbon)	-	0.88	N/A	0.8
S25	Single-atom Fe-N-C	-	0.915	N/A	0.408
S26	Single-atom Fe/N-doped hierarchical porous carbon	-	0.904	84.5	0.51
Present work	FePc-MoS_2	-	0.89	32	0.1

III. Supporting Figures

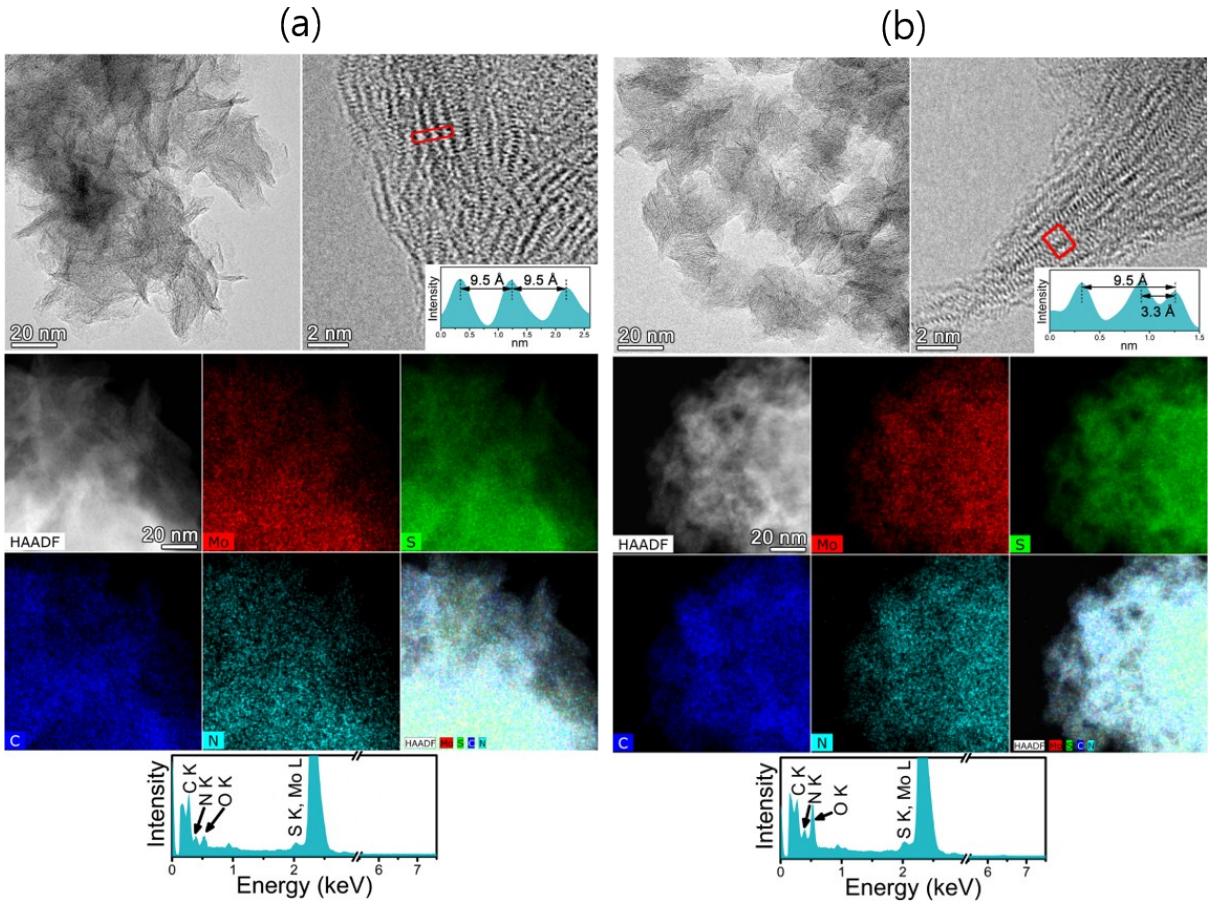

Figure S1. HRTEM, HADDF, and EDX mapping images of (a) MoS_2 and (b) H_2Pc-MoS_2, and corresponding EDX spectrum.

The MoS_2 and H_2Pc-MoS_2 consisted of the flower-like MoS_2 nanosheets that assembled into the porous nanoparticles with the size of 50 nm. The average thickness of the MoS_2 nanosheets was 5 nm. The lattice-resolved TEM image shows that the average distance between adjacent MoS_2 layers (d_{002}) is 9.5 Å, for MoS_2 and H_2Pc-MoS_2. XRD pattern confirmed c = 19 Å for two samples, which is consistent with the TEM images. The intercalated H_2Pc lies at a close distance of 3.3 Å from the MoS_2 layer, which is the same as FePc. In the case of MoS_2, no interlayer is detected between the adjacent MoS_2. The EDX spectrum revealed the homogeneous distribution of the composition (Mo, S, C, and N) in the entire sample.

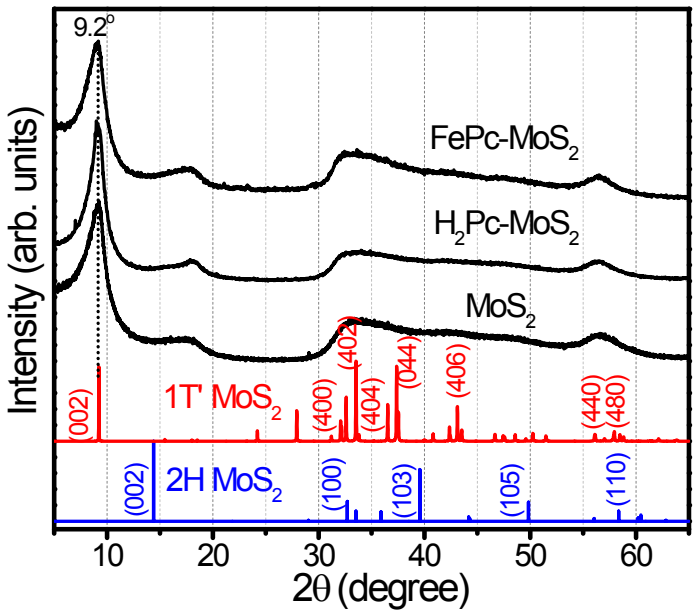

Figure S2. XRD pattern of FePc-MoS_2, H_2Pc-MoS_2, and MoS_2 complexes. The peaks were referenced to those of of 2H phase shown at the bottom (JCPDS No. 87-2416; a = 3.160 Å and c = 12.290 Å) and 1T′ phase MoS_2 (a = 3.27 Å, b = 3.17 Å, and c = 19.0 Å), as shown at the bottom.

VESTA program (http://jp-minerals.org/vesta/en/) was used to generate the simulated XRD pattern for 1T′ phase whose lattice parameters were obtained by the present calculation. The (002) peak of MoS_2 samples is shifted significantly to 9.2°, corresponding to c = 19 Å and in agreement with the TEM data. The broad peaks at 2θ = 32° and 57° are ascribed to the overlapped many peaks.

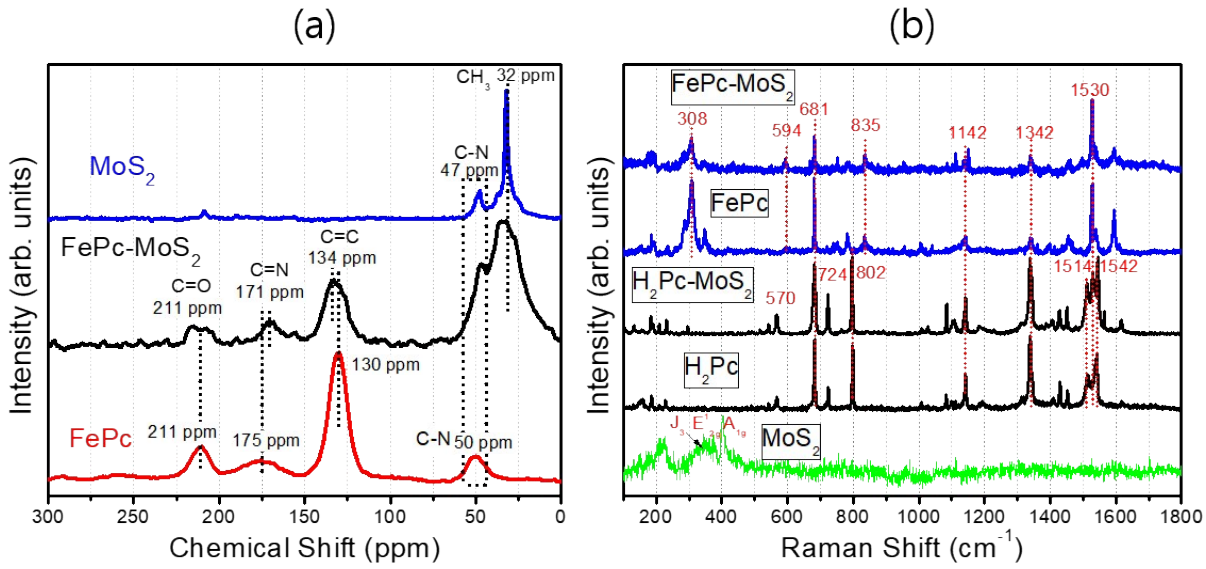

Figure S3. (a) Solid state ^{13}C NMR spectrum and (b) Raman spectrum of MoS_2, FePc, and FePc-MoS_2. The FePc powders was purchased from Sigma-Aldrich.

(a) The ^{13}C NMR spectrum of FePc show the C-N peak at 50 ppm, C=C (sp^2) peak at 130 ppm, C=N (pyrollic and bridge) at 175 ppm, and C=O at 211 ppm. The FePc-MoS_2 shows the peaks of FePc at 134, 171, and 211 ppm. The 4 ppm blueshift of C=C from the peak of FePc could be due to the π electron transfer to MoS_2. The 4 ppm redshift of C=N peaks could be related with the elongated Fe-N distance caused by Fe-S interaction. The peaks at 32 and 47 ppm can be assigned to the C-N and CH_3 of solvent (dimethylformamide), respectively, since the MoS_2 shows the same peaks. Therefore, the NMR data confirm that FePc-MoS_2 samples contain the FePc molecules.

(b) We assigned the Raman peaks of H_2Pc and FePc powders based on the references, as shown below.[S27] The MoS_2 hybrid complexes show the Raman peaks of the matching Pc molecules, indicating that FePc-MoS_2 and H_2Pc-MoS_2 contain the FePc and H_2Pc molecules, respectively. The MoS_2 exhibit two characteristic Raman at 380 and 403 cm^{-1}, corresponding to the in-plane E^1_{2g} and out-of-plane A_{1g} vibration modes, respectively. Raman peaks of 1T' phase: the J_1 peak at 148 cm^{-1}, the J_2 peak at 236 cm^{-1}, and the J_3 peak at 336 cm^{-1}, are not clearly identified probably because of the DMF solvent peaks.[S28] FePc-MoS_2 and H_2P-MoS_2 exhibit negligibly weak MoS_2 peaks due to the stronger peaks of Pc molecules.

Summary of peak assignment

Assignment	FePc and FePc-MoS_2	H_2Pc and H_2Pc-MoS_2
Fe-N stretching	308	--
Benzene ring deformation	594	570
Macrocycle breathing	681	681, 724
Out-of-plane bending	835	802
Pyrrole breathing	1142	1142
C-C stretching	1342	1342
C-N-C stretching	1530	1514, 1530, 1542

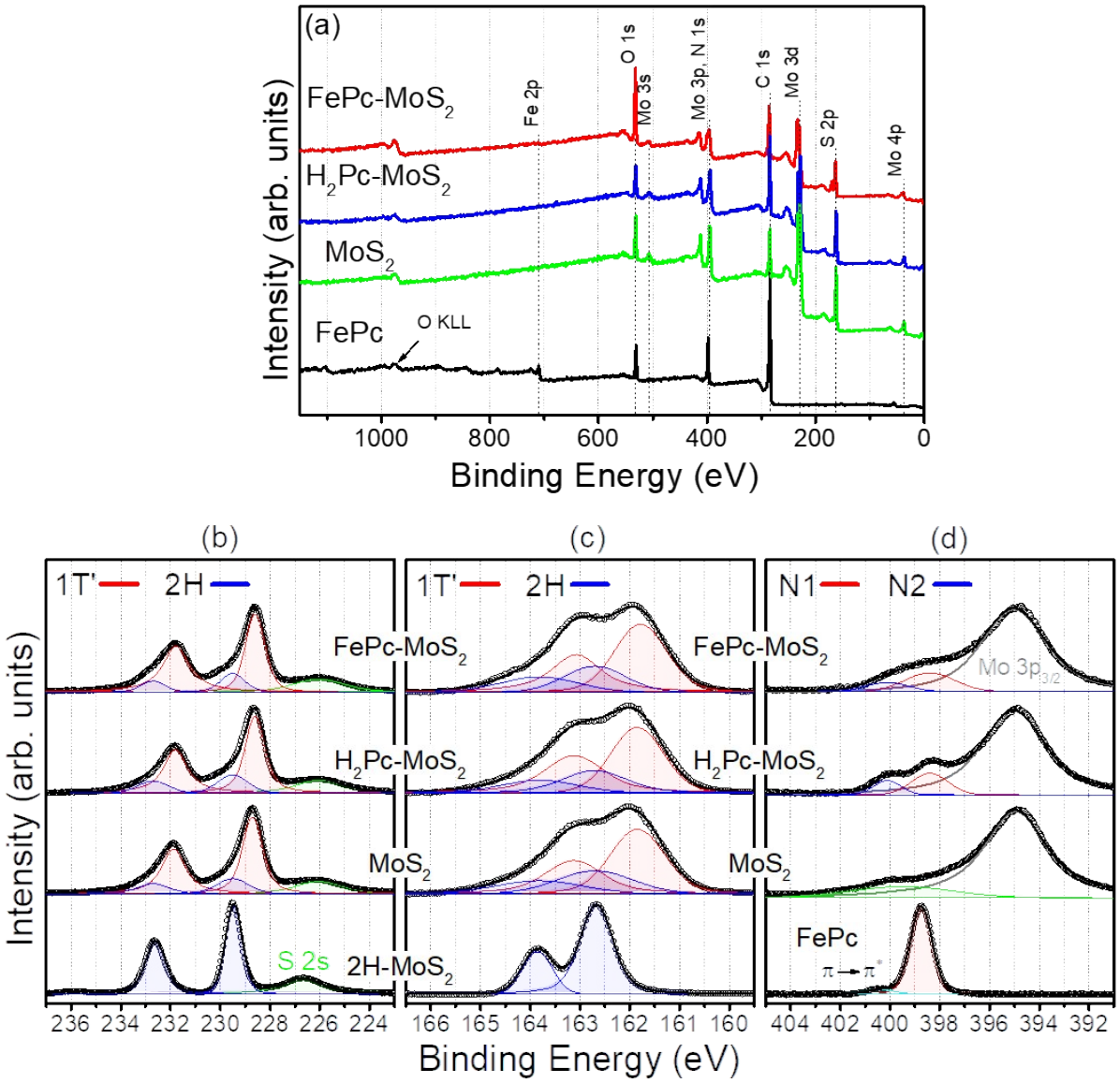

Figure S4. (a) Full-range XPS, and fine-scanned (b) Mo $3d_{3/2}$ and $3d_{5/2}$ peaks, (c) S 2*p* peaks, and (d) N 1s peaks of samples: 2H-MoS_2 bulk powders, MoS_2, H_2Pc-MoS_2, FePc-MoS_2, and FePc powders.

(a) The atomic ratio of [S]/[Mo] is 2 for all MoS_2 samples. For FePc-MoS_2, [Fe]/[Mo] is 5%. The C peak of H_2Pc-MoS_2 and FePc-MoS_2 is larger in the intensity than that of MoS_2 due to the Pc molecules.

(b) The 2H phase MoS_2 powders show the $3d_{5/2}$ peak at 229.5 eV. The peak of MoS_2, H_2Pc-

MoS_2 and FePc-MoS_2 was resolved into two bands: 1T' phase (red) at 228.6 eV and 2H phase (blue) at 229.5 eV. The fraction of the 1T' phase band was determined as 75%, providing an evidence that the 1T' phase is the major phase.

(c) The S $2p_{3/2}$ and S $2p_{1/2}$ peaks, which are separated by about 1.2 eV. The 2H-MoS_2 shows peaks at 162.3 and 163.5 eV, which are 1.7 eV red-shifted with respect to the signal of neutral S (S^0) at 164.0 and 165.2 eV. They correspond to the S^{2-} anions bonded with the Mo cations in the 2H phase. For the three MoS_2 samples, the broad peak was resolved into four bands; two each for the 2H phase (blue) and the 1T' phase (red). The larger red-shift band, S $2p_{3/2}$ at 161.3 eV and S $2p_{1/2}$ at 162.5 eV, are assigned to those of electron-rich 1T' phase.

(d) In the case of MoS_2 samples, Mo $3p_{3/2}$ peak appears at 394.9 eV. The FePc-MoS_2 shows the pyrollic/bridge C-N (N1) peak at 398.5 eV and its positive charged C-N (N2) peak at 400 eV. The H_2Pc-MoS_2 shows the pyrollic/bridge C-N (N1) peak at 398.5 eV and N-H (N2) peak at 400 eV. The MoS_2 shows a broad peak due to the DMF solvent.

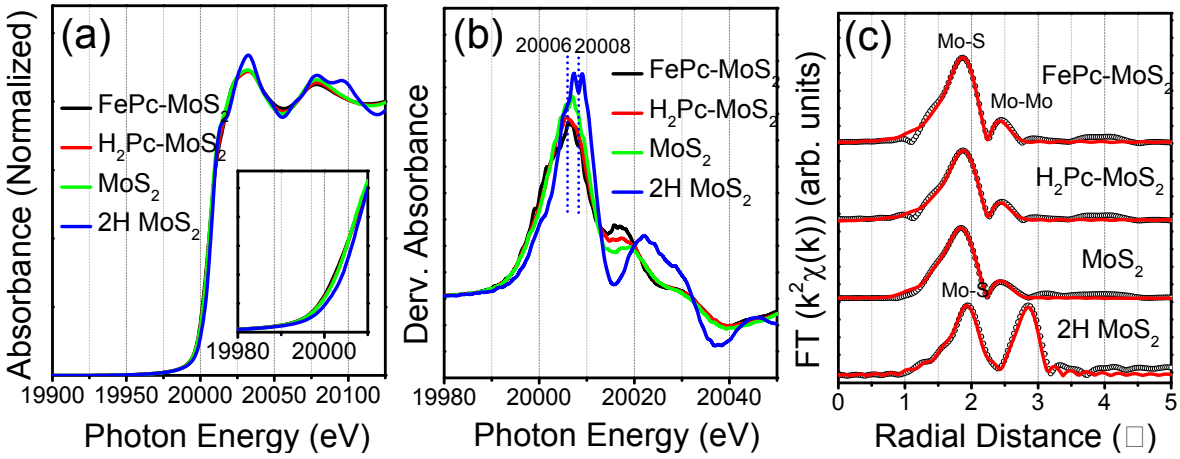

Figure S5. (a) XANES spectra at the Mo K edge for FePc-MoS_2, H_2Pc-MoS_2, MoS_2, and 2H-MoS_2 (bulk powders), (b) First derivative of absorbance curve in the onset region. (c) Non-phase-corrected k^2 weighted FT EXAFS data (open circles) at the Mo K edge and their fitting curves (line).

(a) The evolution of the local crystal structure of MoS_2 upon the intercalation was probed with Mo K-edge X-ray absorption near edge spectra (XANES) analysis. Magnified scaled spectrum (inset) reveals that edge energies of all samples are lower than that of 2H-MoS_2, due to more metallic 1T' phase than 2H phase.

(b) The first derivative of absorption curve in the onset region shows a peak at 20008 eV for 2H phase MoS_2. The 1T' phase MoS_2 samples shows a peak at 20006 eV, indicating the more metallic nature compared to the 2H phase MoS_2.

(b) In the Fourier transform (FT) profiles (in real space) of the extended X-ray absorption fine structure (EXAFS), the peaks indicate the distances to nearest neighbor atoms. The profiles of the FePc-MoS_2, H_2P-MoS_2 and MoS_2 are significantly different from that of 2H-MoS_2, suggesting a remarkable change in the local atomic arrangements. The curves were fitted to two scattering shells, Mo–S and Mo–Mo bonds (see the parameters in **Table S1**). For the 2H

phase MoS_2 bulk powders, the shortest distance of Mo–S (d_{Mo-S}) and Mo–Mo bonds (d_{Mo-Mo}) is 2.40 and 3.16 Å, respectively. The FePc-MoS_2, H_2P-MoS_2, and MoS_2 show d_{Mo-S} = 2.40 Å and d_{Mo-Mo} = 2.76-2.78 Å, corresponding to the value of 1T′ phase. The peak intensity of 1T′ phase decreases by almost 1/3 due to the reduced coordination number of Mo. Therefore, we conclude that all MoS_2 samples adopt a distorted octahedral coordinated 1T′ phase.

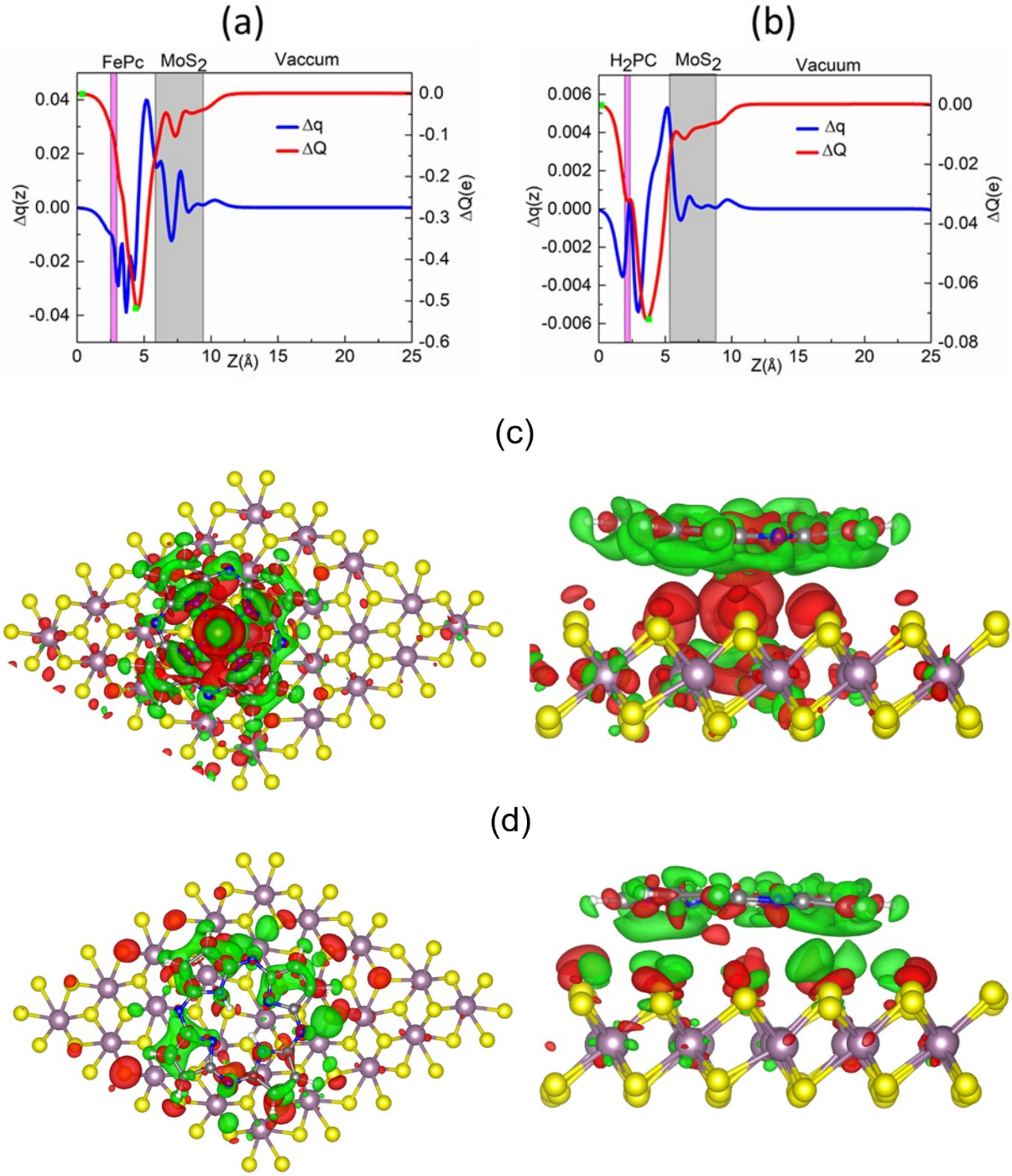

Figure S6. Δq and ΔQ of 1T′ phase (a) (5×5) FePc-MoS_2 and (b) (5×5) H_2Pc-MoS_2 versus z: z_{min} and z_{max} values corresponding to $Q_{min}(z)$ and $Q_{max}(z)$ are shown by filled green squares (■), respectively. Δρ(*x*, *y*, *z*) contour plots (top and side views) for (c) FePc-MoS_2 and (d) H_2Pc-

MoS_2, with a range of -0.023–0.011 and -0.027–0.013 *e* Å^{-3}, respectively. Charge accumulation and depletion regions are represented in red and green colors, respectively.

Following our previous studies, the amount of the charge transfer was calculated.[S3,S29] The change in electron density (expressed in *e* Å^{-3}) along the *c* (= *z*) axis generated by the intercalation process was defined as $\Delta\rho(z) = \rho(z)\{$ FePc (or H_2Pc)-$MoS_2\} - \rho(z)\{MoS_2\} - \rho(z)\{$FePc (or $H_2Pc)\}$, averaged over the *xy* plane in a supercell. The total electron density change (*e*) was defined as $\Delta q(z) = \Delta\rho(z)\Delta V$, where ΔV is the volume of a fine grid, i.e., $\Delta V = V_{cell}/N_c$, in which V_{cell} is the total volume of the supercell and N_c is the number of fine grids. The thickness of the MoS_2 layer was defined on the basis of the *z* coordinates of the S atoms in the upper and lower sublayers (S_L and S_U), with $z(S_L) < z(S_U)$. The thickness of Pc molecules was obtained from the minimum and maximum *z* coordinates of its atoms. The actual thickness might be larger than that obtained using this definition, if the finite atomic size is taken into account. The $Q(z) = \sum_{0}^{z' \le z} \Delta q(z')$, which is the integration of charge difference $\Delta q(z')$ within $z' < z < c$, is displayed on the right vertical axis. The amount of charge transfer was defined as $\Delta Q = Q_{max} - Q_{min}$, where Q_{max} and Q_{min} correspond to the maximum and minimum charge values in the regions (marked by green squares) adjacent to the MoS_2 layers and FePc (or H_2Pc) molecules, respectively. The calculated ΔQ value of FePc-MoS_2 was 0.52*e*, which is larger than that (0.07*e*) of H_2Pc-MoS_2. The larger ΔQ values confirmed that a more significant charge transfer took place in the FePc-MoS_2.

The contour plots for $\Delta\rho(x, y, z)$ were obtained by no integration over the *xy* plan. The charge accumulation and depletion regions were represented in red and green, respectively. The FePc-MoS_2 shows a significant electron transfer from the phenyl ring (as well as amine groups) to the MoS_2 layer. The majority of the transferred electrons are concentrated on the interlayer region. In contrast, H_2Pc-MoS_2 shows a negligible electron transfer.

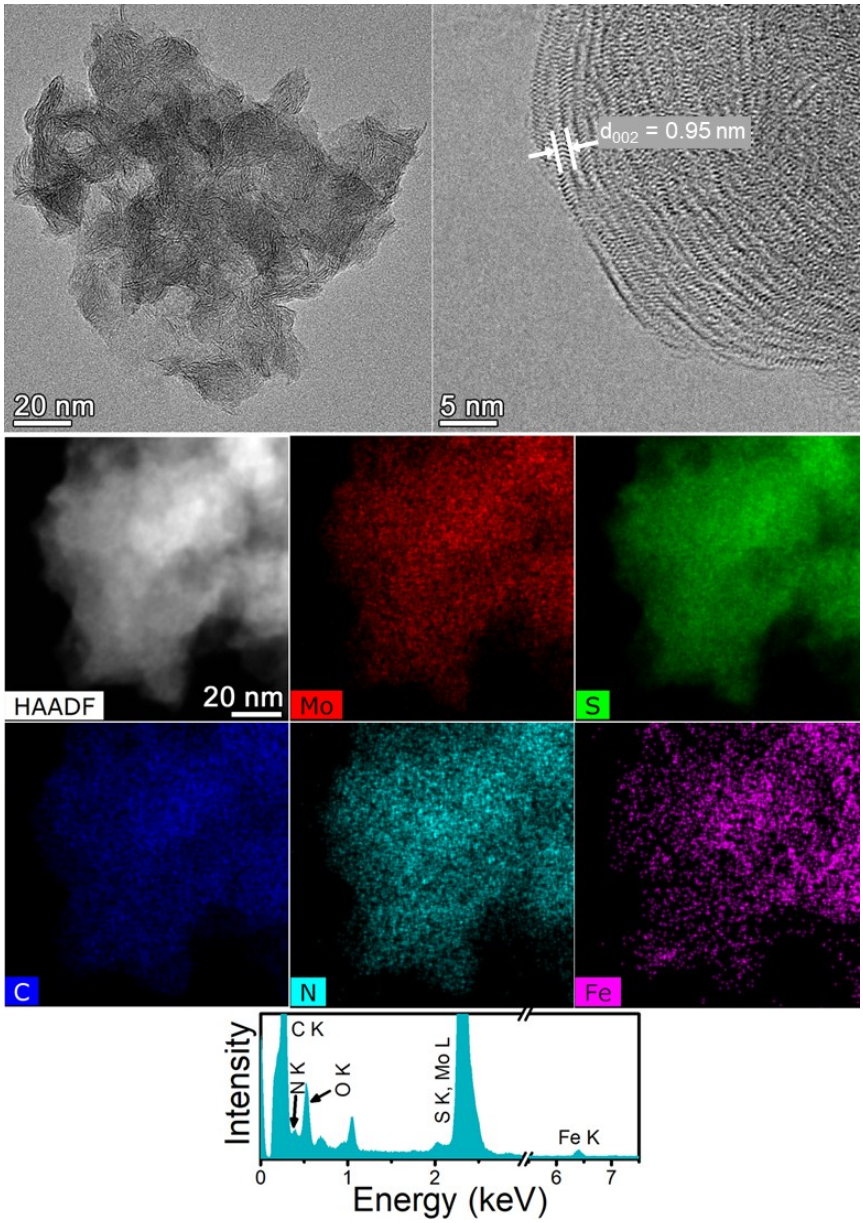

Figure S7. TEM images and EDX data of FePc-MoS_2 after 24 h chronoamperometric measurement of HER.

The average size of nanosheets is 20 nm, which is smaller than that of the samples before HER (50 nm). The lattice-resolved TEM image shows that the average distance between adjacent MoS_2 layers (d_{002}) is the same as that of the before samples; 9.5 Å. The EDX mapping and spectrum show that Mo/S, N, C, and Fe atoms distribute homogeneously over the entire samples. The similar intensity of Fe peak (relative Mo/S peak) as that of before sample was observed.

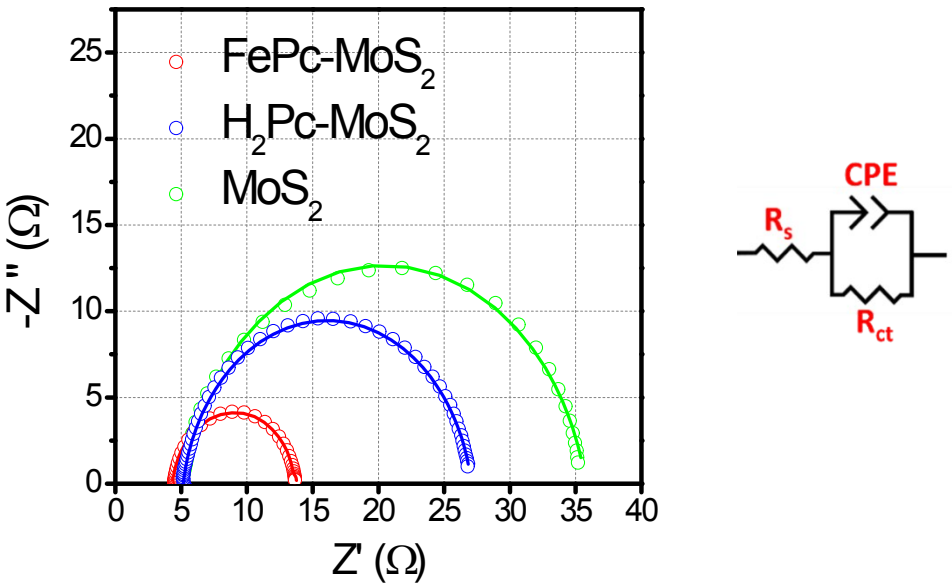

Figure S8. Nyquist plots for EIS measurements of FePc-MoS_2, H_2Pc-MoS_2, and MoS_2 from 100 kHz to 0.1 Hz at a representative potential of -0.15 V (vs. RHE) and the equivalent circuit diagram.

Electrochemical impedance spectroscopy (EIS) measurements were performed in the frequency range of 100 kHz–0.1 Hz and an amplitude of 10 mV at η = 0.15 V. In the high-frequency limit and under non-Faradaic conditions, the electrochemical system is approximated by the modified Randles circuit shown on the right panel, where R_s denotes the solution resistance, CPE is a constant-phase element related to the double-layer capacitance, and R_{ct} is the charge-transfer resistance from any residual Faradaic processes. A semicircle in the low-frequency region of the Nyquist plots represents the charge transfer process, with the diameter of the semicircle reflecting the charge-transfer resistance. The real (Z') and negative imaginary ($-Z''$) components of the impedance are plotted on the x and y axes, respectively. Simulating the EIS spectra using an equivalent circuit model allowed us to determine R_{ct}, which is a key parameter for characterizing the catalyst-electrolyte charge transfer process.

The fitting parameters are listed in **Table S2**. The obtained R_{ct} values are 8.5, 22.2, and 30.0, Ω for FePc-MoS_2, H_2Pc-MoS_2, and MoS_2, respectively. The FePc-MoS_2 samples have much smaller charge transfer resistance (R_{ct}) than others. The order of R_{ct} is consistent with that of the HER performance. The reduced charge-transfer resistance plays a major role in enhancing the HER catalytic activity of the FePc-MoS_2.

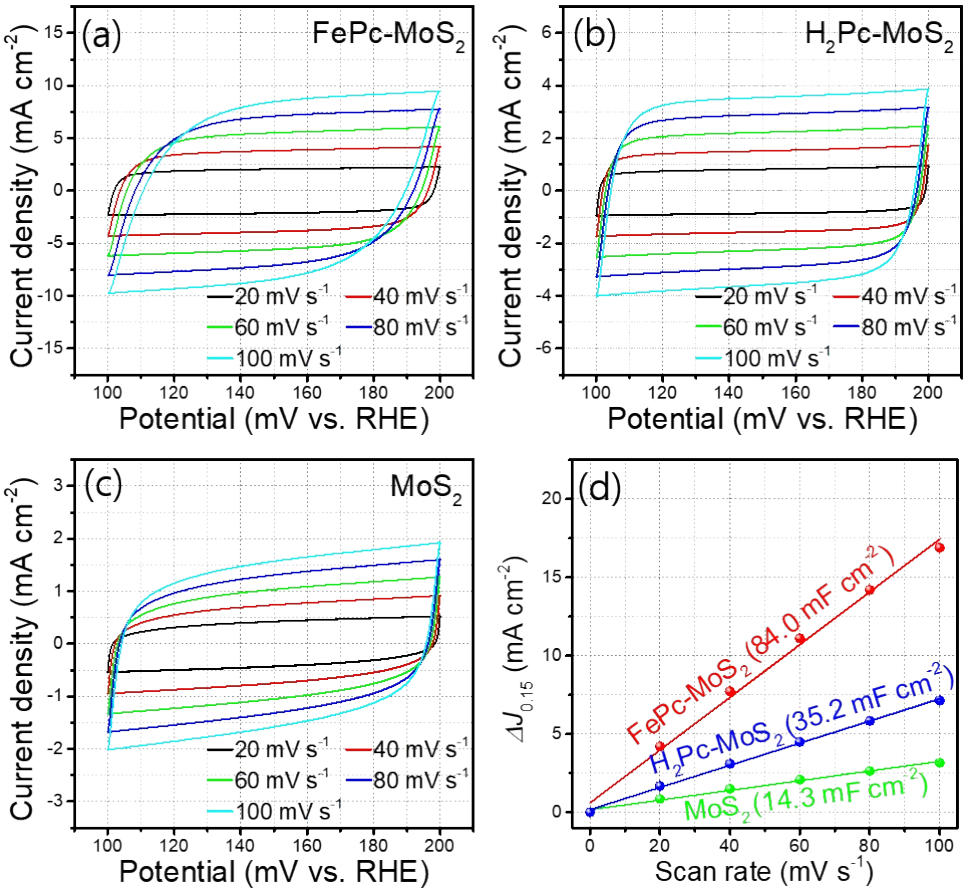

Figure S9. Cyclic voltammograms of (a) FePc-MoS_2, (b) H_2Pc-MoS_2, and (c) MoS_2 in a non-Faradaic region (0.1-0.2 V vs. RHE), at 20–100 mV s^{-1} scan rates and in 0.5 M H_2SO_4 solution. (d) Difference (ΔJ) between the anodic charging and cathodic discharging currents measured at 0.15 V (vs. RHE) and plotted as a function of the scan rate. The value in parenthesis represents the C_{dl}, obtained by the half of the linear slope.

The C_{dl} values of MoS_2, H_2Pc-MoS_2, and FePc-MoS_2 are 14.3, 35.2, and 84.0 mF cm^{-2}, respectively (see the summary in **Table S2**), showing a significant increase upon intercalation. The intercalated MoS_2 samples have very rough surfaces and can thus expose a large number of active sites. Therefore, the increased double-layer capacitance leads to the enhanced HER catalytic activity of the intercalated samples. The C_{dl} values follow the same order as that of HER performance: FePc-MoS_2 > H_2Pc-MoS_2 > MoS_2.

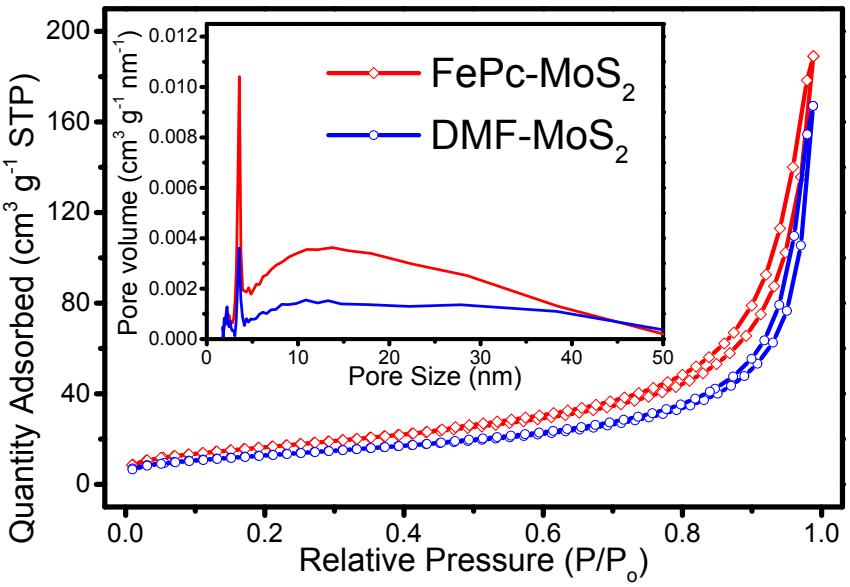

Figure S10. Nitrogen adsorption-desorption isotherm curves and pore size distribution of FePc-MoS_2 and MoS_2 samples. Fitting parameters are summarized in **Table S3**.

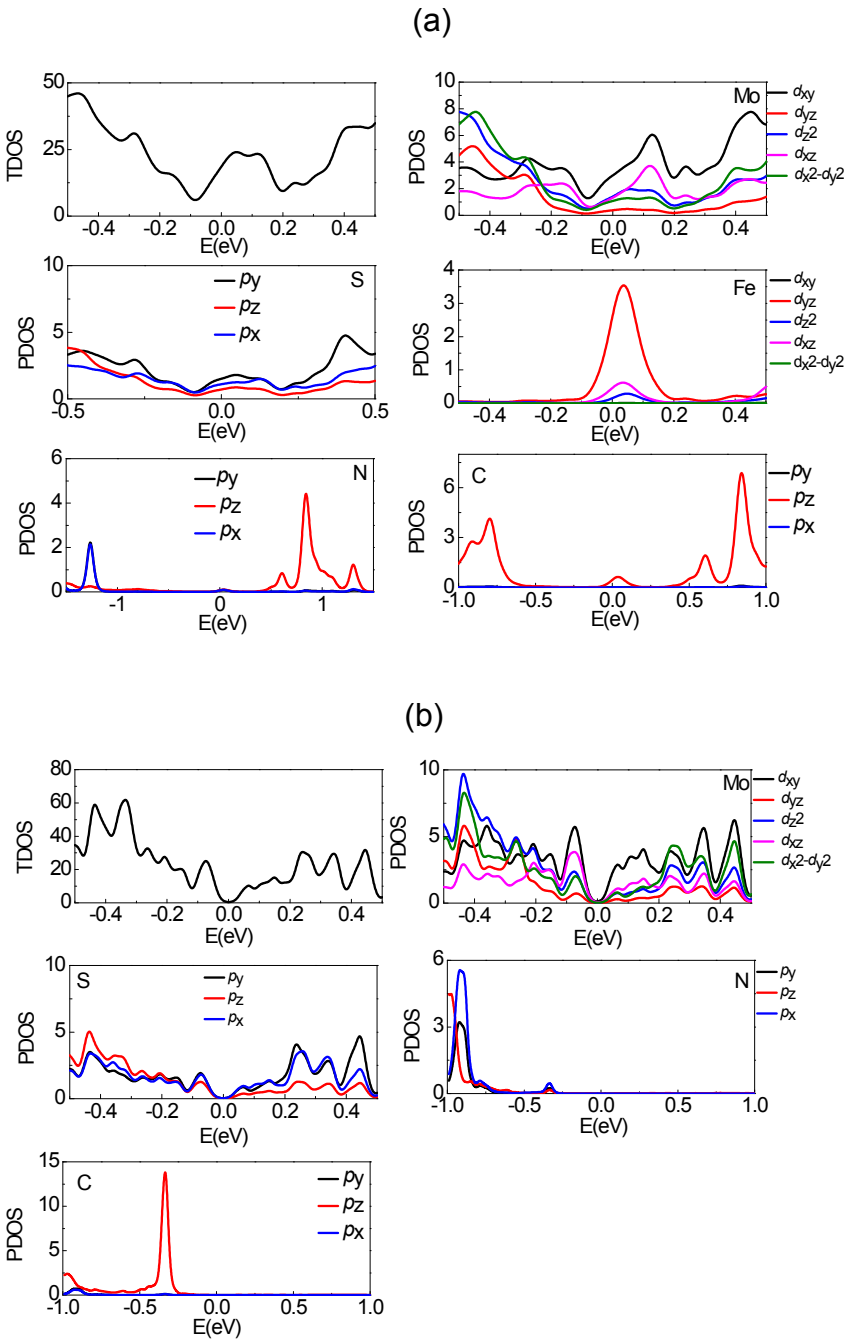

Figure S11. TDOS and PDOS of the constituents (Mo, S, Fe, N, and C) of (a) FePc-MoS_2 and (b) H_2Pc-MoS_2

The total DOS (TDOS) of FePc-MoS_2 shows an enhancement around the Fermi level. To explore the origin, we analyzed the partial DOS (PDOS) of the constituents (Mo, S, Fe, N, and C). The coordinate system is defined in such a way that N atoms of FePc are oriented along the X and Y directions from the Fe ion. Hence, $d_{x^2-y^2}$(Mo) involved in the bonding interaction of

the Fe-N bonds is located far below the Fermi level, while its antibonding interaction is far above. Around the Fermi level, the PDOS shows a hybridization of d_{xy}(Mo), p(S), and d_{yz}(Fe) states, being responsible for Mo-S and Fe-S bonds. In the H_2Pc-MoS_2, the TDOS around the Fermi level is much smaller than that of FePc-MoS_2. Since there is no Fe d state in the H_2Pc, the PDOS of d_{xy}(Mo) and p(S) states becomes much smaller. This result shows that Fe center plays an important role in enhancing only the TDOS but also the PDOS around the Fermi level.

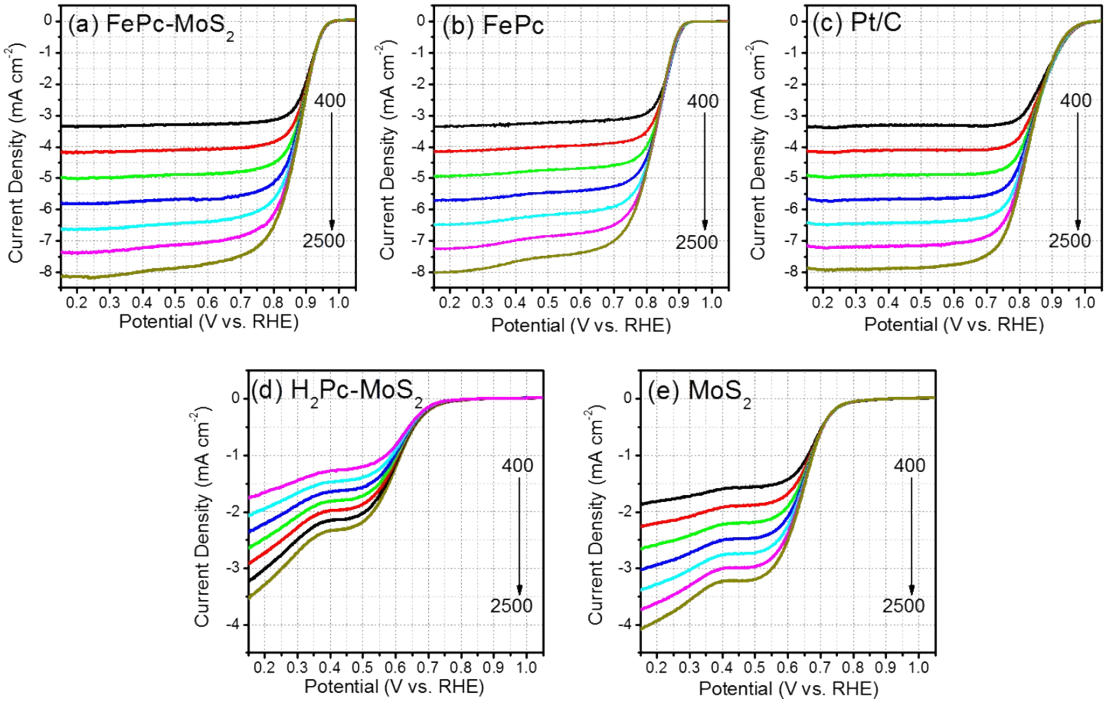

Figure S12. The LSV curves of ORR at various rotation speeds (400, 625, 900, 1225, 1600, 2025, and 2500 ppm); (a) FePc-MoS_2, (b) FePc, (c) Pt/C, (d) H_2Pc-MoS_2, and (e) MoS_2.

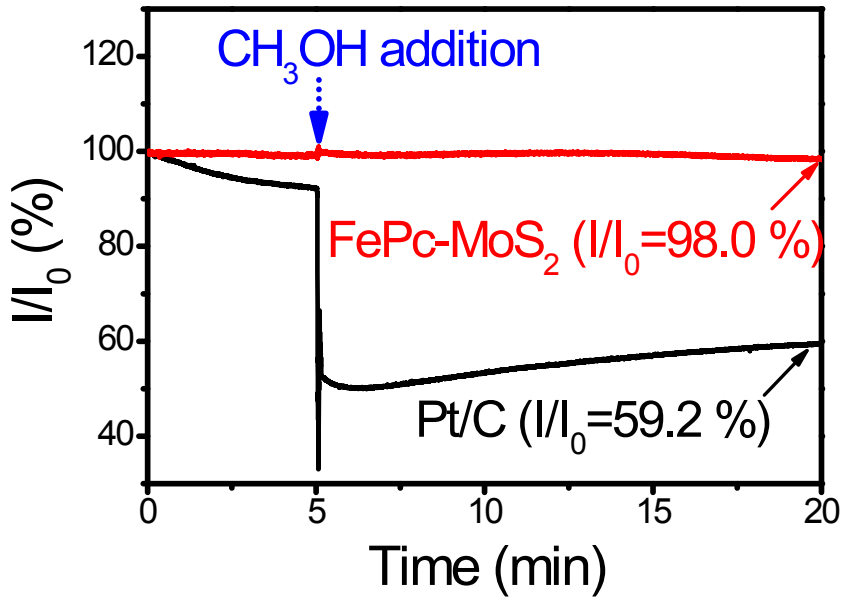

Figure S13. ORR current vs. time (min) at applied voltage of -0.2 V. Arrow indicates the addition of 3.0 M methanol (MeOH) into O_2-saturated electrochemical cell.

For FePc-MoS_2, there is 8% decrease in O_2 reduction current upon the addition of MeOH in the O_2-saturated 0.1 M KOH solution, showing electrocatalytic selectivity for O_2 that evades the crossover effect of alcohol. However, the CV curve of the Pt/C shows a dramatic decrease of current when the 3M MeOH is added under the same condition. It indicates that FePc-MoS_2 holds high promise for use as cathode in methanol and alkaline fuel cells.

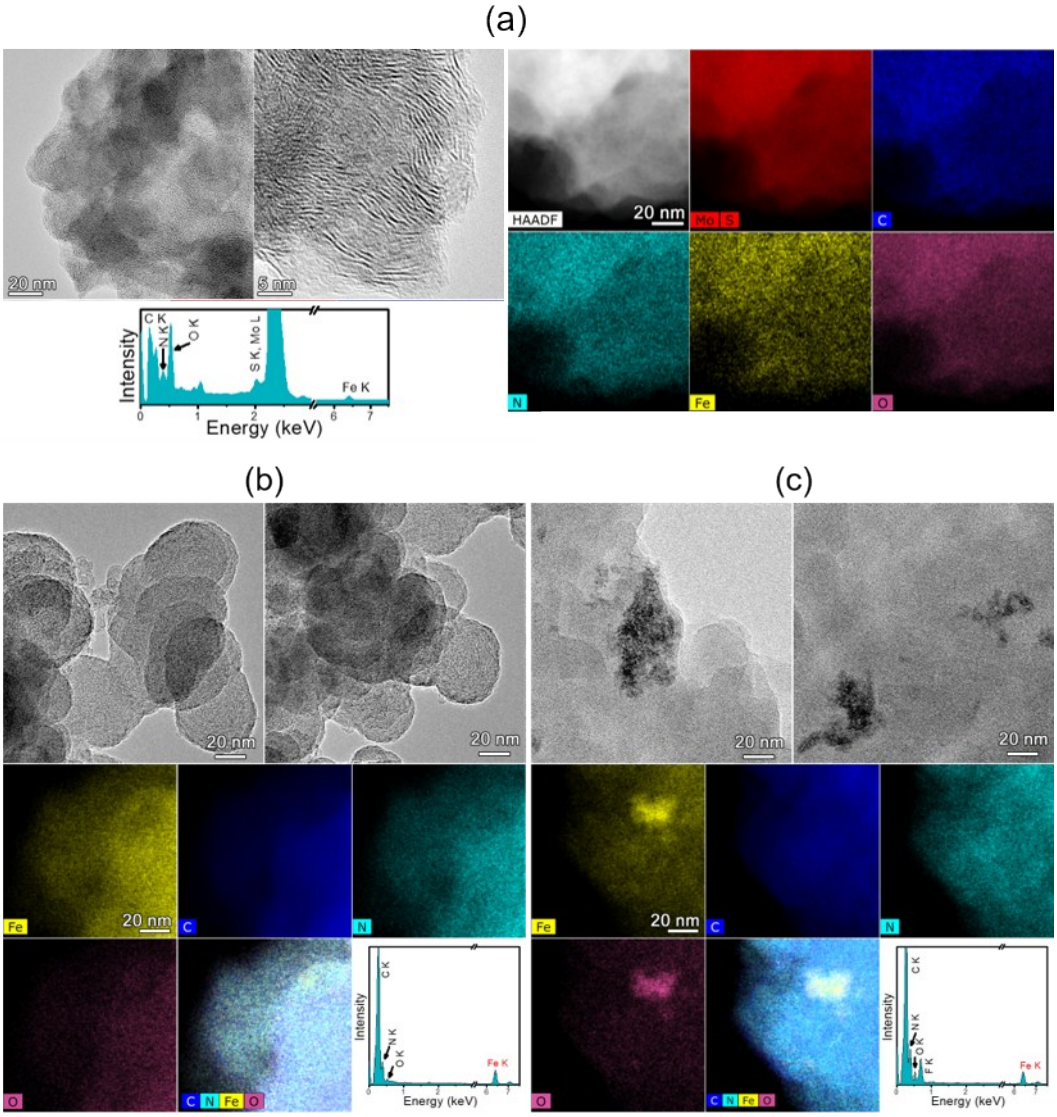

Figure S14. HRTEM images of (a) FePc-MoS_2 after 20 h ORR and FePc (dispersed in carbon black) (b) before and (c) after 20 h ORR; EDX mapping of Mo (L shell),S (K shell), Fe (K shell), C (K shell), N (K shell), and O (K shell) and the corresponding EDX spectra.

HRTEM images and EDX elemental mapping (Mo L shell, S K shell, Fe K shell, C K shell, N K shell, O K shell), and the corresponding EDX spectra for FePc-MoS_2 (after 20 h ORR) shows that the nanosheets consisted of the expanded MoS_2 layers and all elements distribute over whole nanosheets with 5% Fe composition. In the case of FePc sample, the aggregated nanoparticles are produced after ORR. The EDX data shows that Fe element is distributed homogeneously before ORR, but becomes localized after ORR, probably due to the formation of Fe oxide nanoparticles.

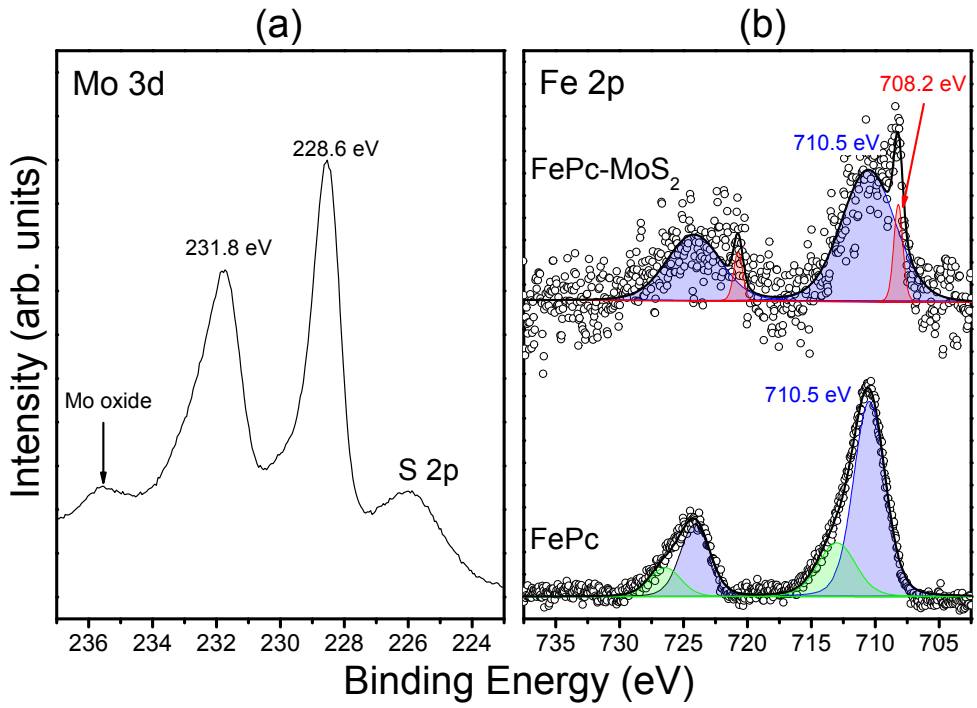

Figure S15. Fine-scanned XPS (a) Mo 3d and (b) Fe 2p peaks of FePc-MoS_2 and FePc (dispersed in carbon black) after 20 h ORR.

The Mo $3d_{3/2}$ and $3d_{5/2}$ peaks at 228.6 and 231.8 eV, respectively, shows that the 1T′ phase of FePc-MoS_2 retains after ORR. The Mo-O peak at 235.6 eV appears due to the oxidation.

The Fe $2p_{3/2}$ $2p_{3/2}$ peak of FePc-MoS_2 consisted of Fe(II)-N at 708.2 eV and Fe(III)-N/Fe-O at 710.6 eV. The intensity of Fe(III)-N/Fe-O peak increases after ORR. The FePc sample shows the peaks at 710.5 and 713.1 eV, which are close to those of Fe_2O_3, due to the formation of oxide nanoparticles as shown in **Figure S14**.

IV. References

S1. C. C. L. McCrory, S. Jung, I. M. Ferrer, S. M. Chatman, J. C. Peters and T. F. Jaramillo, *J. Am. Chem. Soc.*, 2015, **137**, 4347-4357.

S2. Y. Yin, J. Han, Y. Zhang, X. Zhang, P. Xu, Q. Yuan, L. Samad, X. Wang, Y. Wang, Z. Zhang, P. Zhang, X. Cao, B. Song and S. Jin, *J. Am. Chem. Soc.*, 2016, **138**, 7965-7972.

S3. I. S. Kwon, I. H. Kwak, H. G. Abbas, G. Jung, Y. Lee, J. Park, S. J. Yoo, J. G. Kim and H. S. Kang, *Nanoscale*, 2018, **10**, 11349-11356.

S4. J. Xie, H. Zhang, S. Li, R. Wang, X. Sun, M. Zhou, J. Zhou, X. W. Lou and Y. Xie, *Adv. Mater.,* 2013*,* **25***,* 5807-5813.

S5. D. Voiry, M. Salehi, R. Silva, T. Fujita, M. Chen, T. Asefa, V. B. Shenoy, G. Eda and M. Chhowalla, *Nano Lett.,* 2013, **13**, 6222-6227.

S6. Z. Wu, C. Tang, P. Zhou, Z. Liu, Y. Xu, D. Wang and B. Fang, *J. Mater. Chem. A,* 2015, **3**, 13050-13056.

S7. D. Voiry, R. Fullon, J. Yang, C. C. C. Silva, R. Kappera, I. Bozkurt, D. Kaplan, M. J. Lagos, P. E. Batson, G. Gupta, A. D. Mohite, L. Dong, D. Er, V. B. Shenoy, T. Asefa and M. Chhowalla, *Nat. Mater.,* 2016*,* **15***,* 1003-1009.

S8. X. Geng, W. Sun, W. Wu, B. Chen, A. A. Hilo, M. Benamara, H. Zhu, F. Watanabe, J. Cui and T. Chen, *Nat. Commun.,* 2016, **7**, 10672.

S9. J. Zhang, J. Wu, H. Guo, W. Chen, J. Yuan, U. Martinez, G. Gupta, A. Mohite, P. M. Ajayan and J. Lou, *Adv. Mater.,* 2017*,* **29***,* 1701955.

S10. D. Wang, X. Zhang, S. Bao, Z. Zhang, H. Fei and Z. Wu, *J. Mater. Chem. A,* 2017, **5**, 2681-2688.

S11. E. E. Benson, H. Zhang, S. A. Schuman, S. U. Nanayakkara, N. D. Bronstein, S. Ferrere, J. L. Blackburn and E. M. Miller, *J. Am. Chem. Soc.,* 2018, **140***,* 441-450.

S12. C. Tan, Z. Luo, A. Chaturvedi, Y. Cai, Y. Du, Y. Gong, Y. Huang, Z. Lai, X. Zhang, L. Zheng, X. Qi, M. H. Goh, J. Wang, S. Han, X. J. Wu, L. Gu, C. Kloc and H. Zhang, *Adv. Mater*., 2018, **30***,* 1705509.

S13. L. Lin, N. Miao, Y. Wen, S. Zhang, P. Ghosez, Z. Sun and D. A. Allwood, *ACS Nano*, 2016, **10**, 8929-8937.

S14. C. Tsai, H. Li, S. Park, J. Park, H. S. Han, J. K. Nørskov, X. Zheng and F. Abild-Pedersen, *Nat. Commun*., 2017, **8**, 15113.

S15. Y. Shi, Y. Zhou, D. R. Yang, W. X. Xu, C. Wang, F. B. Wang, J. J. Xu, X. H. Xia and H. Y. Chen, *J. Am. Chem. Soc.*, 2017, **139**, 15479−15485

S16. Z. Luo, Ouyang, Y.; Zhang, H.; Xiao, M.; Ge, J.; Jiang, Z.; J. Wang, D. Tang, X. Cao, C. Liu and W. Xing, *Nat. Commun*., 2018, **9**, 2120.

S17. I. S. Amiinu, Z. Pu, X. Liu, K. A. Owusu, H. G. R. Monestel, F. O. Boakye, H. Zhang and S. Mu, *Adv. Funct. Mater.* 2017, **27**, 1702300

S18. C. Zhao, Y. Zhang, L. Chen, C. Yan, P. Zhang, J. M. Ang and X. Lu, *ACS Appl. Mater. Interfaces* 2018, **10**, 23731-23739.

S19. R. Cao, R. Thapa, H. Kim, X. Xu, M. G. Kim, Q. Li, N. Park, M. Liu and J. Cho, *Nat. Commun.* 2013, **4**, 2076.

S20. J. Yang, F. Toshimitsu, Z. Yang, T. Fujigaya and N. Nakashima, *J. Mater. Chem. A* 2017, **5**, 1184-1191.

S21. Z. Zhang, M. Dou and J. Ji, F. Wang, *Nano Energy* 2017, **34**, 338-343.

S22. Z. Li, Z. Zhuang, F. Lv, H. Zhu, L. Zhou, M. Luo, J. Zhu, Z. Lang, S. Feng, W. Chen, L. Mai and S. Guo, *Adv. Mater.* 2018, **30**, 1803220.

S23. A. Pizzarro, G. Abarca, C. Gutiérrez-Cerón, D. Cortés-Arriagada, F. Bernardi, C. Berrios, J. F. Silva, M. C. Rezende, J. H. Zagal, R. Oñate and Ingrid Ponce, *ACS Catal*. 2018, **8**, 8406-8419.

S24. Y. J. Sa, D. J. Seo, J. Woo, J. T. Lim, J. Y. Cheon, S. Y. Yang, J. M. Lee, D. Kang, T. J. Shin, H. S. Shin, H. Y. Jeong, C. S. Kim, M. G. Kim, T. Y. Kim and S. H. Joo, *J. Am. Chem. Soc*. 2016, **138**, 15046-15056.

S25. R. Jiang, L. Li, T. Sheng, G. Hu, Y. Chen and L. Wang, *J. Am. Chem. Soc*. 2018, **140**, 11594-11598.

S26. K. Wu, X. Chen, S. Liu, Y. Pan, W. C. Cheong, W. Zhu, X. Cao, R. Shen, W. Chen, J. Luo, W. Yan, L. Zheng, Z. Chen, D. Wang, Q. Peng, C. Chen and Y. Li, *Nano Res*. 2018, **11**, 6260-6269.

S27. A. Kumar, D. Naumenko, L. Cozzarini, L. Barba, A. Cassetta and M. Pedio, *J. Raman Spectrosc*., 2018, **49**, 1015−1022.

S28. D. Yang, S. J. Sandoval, W. M. R. Divigalpitiya, J. C. Irwin and R. F. Frindt, *Phys. Rev. B*, 1991, **43**, 12053-12056.

S29. I. H. Kwak, I. S. Kwon, H. G. Abbas, G. Jung, Y. Lee, T. T. Debela, S. J. Yoo, J. G. Kim, J. Park and H. S. Kang, *Nanoscale*, 2018, **10**, 14726-14735.